The locations of features in the mass distribution of merging binary black holes are robust against uncertainties in the metallicity-dependent cosmic star formation history.

L. A. C. VAN SON, 1,2,3 S. E. DE MINK, 3,2,1 M. CHRUŚLIŃSKA, C. CONROY, R. PAKMOR, AND L. HERNQUIST

¹Center for Astrophysics | Harvard & Smithsonian, 60 Garden St., Cambridge, MA 02138, USA

²Anton Pannekoek Institute of Astronomy, Science Park 904, University of Amsterdam, 1098XH Amsterdam, The Netherlands ³Max Planck Institute for Astrophysics, Karl-Schwarzschild-Str. 1, 85748 Garching, Germany

ABSTRACT

New observational facilities are probing astrophysical transients such as stellar explosions and gravitational wave (GW) sources at ever increasing redshifts, while also revealing new features in source property distributions. To interpret these observations, we need to compare them to predictions from stellar population models. Such models require the metallicity-dependent cosmic star formation history (S(Z,z)) as an input. Large uncertainties remain in the shape and evolution of this function. In this work, we propose a simple analytical function for S(Z,z). Variations of this function can be easily interpreted, because the parameters link to its shape in an intuitive way. We fit our analytical function to the star-forming gas of the cosmological TNG100 simulation and find that it is able to capture the main behaviour well. As an example application, we investigate the effect of systematic variations in the S(Z,z) parameters on the predicted mass distribution of locally merging binary black holes (BBH). Our main findings are: I) the locations of features are remarkably robust against variations in the metallicity-dependent cosmic star formation history, and II) the low mass end is least affected by these variations. This is promising as it increases our chances to constrain the physics that governs the formation of these objects.

1. INTRODUCTION

A myriad of astrophysical phenomena depend criti-23 cally on the rate of star formation throughout the cos-24 mic history of the Universe. Exotic transient phenom-25 ena, including (pulsational) pair-instability supernovae, 26 long gamma-ray bursts and gravitational wave (GW) 27 events appear to be especially sensitive to the metallic-28 ity at which star formation occurs at different epochs 29 throughout the Universe (e.g., ???). Gravitational as-30 tronomy in particular has seen explosive growth in the 31 number of detections in the past decade (???), while 32 theoretical predictions vary greatly due to uncertainties 33 in the aforementioned metallicity of star formation (e.g., 34 ??). In order to correctly model and interpret these ob-35 servations, it is thus fundamental to know the rate of 36 star formation at different metallicities throughout cos-37 mic history; i.e. the metallicity-dependent cosmic star 38 formation history (S(Z, z)), see also the recent review by

Corresponding author: L. van Son lieke.van.son@cfa.harvard.edu

10

11

12

13

14

15

16

17

18

19

20

21

³⁹ ?). Throughout this work little z refers to the redshift and Z to the metallicity of star formation.

It is difficult to observationally constrain the shape of S(Z,z) – (see e.g., ??, for discussion of relevant observational caveats). Even at low redshifts, the low metallicity part of the distribution is poorly constrained (?). Nonetheless, several methods exist to estimate the metallicity-dependent cosmic star formation history.

The first method is based on empirical scaling relations, linking galaxy properties like stellar mass M_{\star} , metallicity Z, and overall star-formation rate density SFRD(z), with the galaxy stellar mass function, GSMF (see e.g. ?). However, the applied methods to infer galaxy properties and subsequently scaling relations such as the MZ-relation differ greatly, which makes it difficult to interpret these results in a consistent way (e.g., ???). Moreover, observations are generally incomplete at high redshifts and low galaxy luminosity (e.g., ??).

One can also directly extract the metallicitydependent cosmic star formation history from cosmological simulations (e.g. ??). However, these simulations
currently lack the resolution to resolve the lowest mass
glalaxies, and their variations in S(Z, z) span a smaller

⁶³ range than those observed in observationally-based mod-⁶⁴ els (?).

Alternatively, one can combine analytical models for the observed overall star-formation rate density, FRD(z), like those from ? or ?, and convolve this with an assumed function for the shape of the cosmic metallicity density distribution, such as was was done to in e.g., ? and the phenomenological model in ?.

In this work we follow the latter approach and propose a flexible analytical model for $\mathcal{S}(Z,z)$ that can be fit to the output of both cosmological simulations, and observational data constraints where available. In contrast to earlier work, we adopt a skewed-lognormal distribution of metallicities that can capture the asymmetry in the low and high metallicity tails.

The purpose of this proposed form is twofold. First 79 of all, the form we propose allows for an intuitive inter-80 pretation of the free parameters. This allows us to get 81 better insight of the impact of changes in these param-82 eters on the inferred ranges of astrophysical transients 83 (as we demonstrate in Section 4 using GW predictions as 84 an example). By adopting an analytical, parametrized form for $\mathcal{S}(Z,z)$, the large uncertainties can be system-86 atically explored. Secondly, both the large complica-87 tions in observational constraints, and the many uncer-88 tainties in cosmological simulations call for a generalised ₈₉ form of $\mathcal{S}(Z,z)$ that can be easily updated when new in-90 formation becomes available. In particular, the advent 91 of observations with the James Webb Space Telescope 92 promises a new era of high-redshift metallicity studies 93 of previously unexplored regimes (e.g., ?). We hope 94 that this form will facilitate the flexibility needed to 95 keep up with observations. The model described in ₉₆ this work is incorporated in the publicly available 'Cosmic Integration' suite of the COMPAS code.1

We describe our model for $\mathcal{S}(Z,z)$ in Section 2. We 99 fit our model to the star-forming gas in the Illustris TNG100 simulation in Section 3, and demonstrate an example application of our model by systematically varying the parameters that determine the shape of $\mathcal{S}(Z,z)$ and investigate their impact on the local distribution of merging BBH masses in Section 4. We summarise our findings in Section 5.

Throughout this work, we adopt a universal Kroupa initial mass function (?) with the mass limits 0.01-1000 0.00 and a flat Λ CDM cosmology with $\Omega_{\rm M}=0.31$, $\Omega_{\Lambda}=0.69$ and $\Omega_{\Lambda}=0.69$

2. A CONVENIENT ANALYTIC EXPRESSION FOR THE METALLICITY-DEPENDENT COSMIC STAR FORMATION HISTORY

110

111

We assume that the metallicity-dependent cosmic star formation history can be separated into two independent functions (as was assumed in e.g., ?, but cf. ? for a discussion on the validity on this assumption).

$$S(Z,z) = SFRD(z) \times \frac{dP}{dZ}(Z,z).$$
 (1)

¹¹⁸ The first term is the star formation rate density, ¹¹⁹ SFRD(z), that is the amount of mass formed in stars ¹²⁰ per unit time and per unit comoving volume at each ¹²¹ redshift, z. The second term, $\mathrm{dP}/\mathrm{dZ}(Z,z)$, is a probability density distribution that expresses what fraction ¹²³ of star formation occurs at which metallicity, Z, at each ¹²⁴ redshift.

2.1. The cosmic metallicity density distribution

For the probability distribution of metallicities we draw inspiration from the approach by e.g., ? who used a log-normal distribution for their phenomenological model. Unfortunately, a simple log-normal distribution cannot capture the asymmetry that we see in the cosmological simulations, which show an extended tail in $\log_{10} Z$ towards low metallicity, combined with a very limited tail towards higher metallicity. To capture this behaviour we adopt a skewed-log-normal distribution instead. This is an extension of the normal distribution that introduces an additional shape parameter, α , that regulates the skewness (first introduced by ?).

The skewed-log-normal distribution of metallicities is defined as:

$$\frac{\mathrm{dP}}{\mathrm{dZ}}(Z,z) = \frac{1}{Z} \times \frac{\mathrm{dP}(Z,z)}{\mathrm{d}\ln Z}$$

$$= \frac{1}{Z} \times \frac{2}{\omega} \underbrace{\phi\left(\frac{\ln Z - \xi}{\omega}\right)}_{(a)} \underbrace{\Phi\left(\alpha \frac{\ln Z - \xi}{\omega}\right)}_{(b)}, \quad (2)$$

where (a) is the standard log-normal distribution, ϕ ,

$$\phi\left(\frac{\ln Z - \xi}{\omega}\right) \equiv \frac{1}{\sqrt{2\pi}} \exp\left\{-\frac{1}{2} \left(\frac{\ln Z - \xi}{\omega}\right)^2\right\}$$
 (3)

¹⁴⁴ and (b) is the new term that allows for asymmetry, which is equal to the cumulative of the log-normal dis-¹⁴⁵ tribution, Φ ,

$$\Phi\left(\alpha \frac{\ln Z - \xi}{\omega}\right) \equiv \frac{1}{2} \left[1 + \operatorname{erf}\left\{\alpha \frac{\ln Z - \xi}{\omega \sqrt{2}}\right\} \right]. \tag{4}$$

This introduces three parameters, α, ω and ξ , each of which may depend on redshift. The first parameter, α ,

 $^{^1}$ https://github.com/TeamCOMPAS/COMPAS/tree/dev/utils/CosmicIntegration

 150 is known as the "shape". It affects the skewness of the 151 distribution and thus allows for asymmetries between 152 metallicities that are higher and lower than the mean. 153 The symmetric log-normal distribution is recovered for 154 $\alpha=0$. The second parameter, ω is known as the "scale". 155 It provides a measure of the spread in metallicities at 156 each redshift. Finally, ξ , is known as the "location", 157 because this parameter plays a role in setting the mean 158 of the distribution at each redshift.

The location and the mean of the metallicity distribution—
160 To obtain a useful expression for the redshift dependence
161 of the "location" $\xi(z)$ we first express the expectation
162 value or mean metallicity at a given redshift

$$\langle Z \rangle = 2 \exp\left(\xi + \frac{\omega^2}{2}\right) \Phi\left(\beta \,\omega\right) \tag{5}$$

where β is

$$\beta = \frac{\alpha}{\sqrt{1 + \alpha^2}}. (6)$$

166 (For a more extended derivation of the moments of the 167 skewed-log-normal, see e.g., ?.)

For the evolution of the mean metallicity with redshift we follow? and the phenomenological model from?

170 in assuming that the mean of the probability density function of metallicities evolves with redshift as:

$$\langle Z \rangle \equiv \mu(z) = \mu_0 \cdot 10^{\mu_z \cdot z},\tag{7}$$

where μ_0 is the mean metallicity at redshift 0, and μ_z determines redshift evolution of the location. Equating this to Equation 5, we get an expression for $\xi(z)$,

$$\xi(z) = \ln\left(\frac{\mu_0 \cdot 10^{\mu_z \cdot z}}{2\Phi(\beta\omega)}\right) - \frac{\omega^2}{2}.$$
 (8)

The scale (and variance) of the metallicity distribution—
178 We will also allow the "scale" ω to evolve with redshift
179 in a similar manner,

$$\omega(z) = \omega_0 \cdot 10^{\omega_z \cdot z}. \tag{9}$$

where ω_0 is the width of the metallicity distribution at z=0, and ω_z the redshift evolution of the scale.

Note that the width, w(z) is not the same as the variance. The variance, $\sigma^2(z)$, can be expressed as

$$\sigma^2(z) = \omega^2(z) \left(1 - \frac{2\beta^2}{\pi} \right) \tag{10}$$

186 Asymmetry of the metallicity distribution: α —The skew-187 ness α could in principle also be allowed to evolve with 188 redshift (e.g., $\alpha(z) = \alpha(z=0)10^{\alpha_z \cdot z}$). However, we find 189 no significant improvement over the simpler assumption 190 where alpha is kept constant. Note that the redshift 191 evolution of the 'scale' (eq. 9), already captures similar behaviour in our current formalism. We therefore adopt $\alpha = \alpha(z=0)$ and $\alpha_z = 0$.

In summary, Equation 2 becomes:

$$\frac{\mathrm{dP}}{\mathrm{dZ}}(Z,z) = \frac{2}{\omega(z)Z} \times \phi\left(\frac{\ln Z - \xi(z)}{\omega(z)}\right) \Phi\left(\alpha \frac{\ln Z - \xi(z)}{\omega(z)}\right) \tag{11}$$

where $\xi(z)$ and $\omega(z)$ are defined in Equations 8 and 9 respectively and we have assumed α to be constant.

2.2. The overall cosmic star formation rate density

For the star formation rate density, we assume the

For the star formation rate density, we assume the analytical form proposed by ?,

SFRD(z) =
$$\frac{d^2 M_{SFR}}{dt dV_c}(z) = a \frac{(1+z)^b}{1 + [(1+z)/c]^d}$$
 (12)

 $_{202}$ in units of $[{
m M}_{\odot}\,{
m yr}^{-1}\,{
m cMpc}^{-3}]$. This introduces four parameters: a which sets the overal normalisation and which has the same units as SFRD(z) and b,c and d which are unitless and which govern the shape of the overal cosmic star formation rate density with redshift.

Lastly, we combine equations 11 and 12 to form a full metallicity specific star formation rate density as described in equation 1.

211 3. FIT AGAINST COSMOLOGICAL SIMULATION

We fit our new functional form of S(Z,z) as defined by equations 1, 11 and 12 to the IllustrisTNG cosmological simulations. We simultaneously fit for the following nine free parameters $\alpha, \mu_0, \mu_z, \omega_0, \omega_z$, which govern the metallicity dependence and a,b,c and d, which set the overall star-formation rate density. Below we briefly discuss the IllustrisTNG simulations, and elaborate on our fitting procedure.

3.1. IllustrisTNG Cosmological simulations

220

Although here, we only fit our model to the TNG100 simulation, our prescription can be easily be used to fit other simulated or observational data of the metallicity-dependent cosmic star formation history².

The IllustrisTNG-project (or TNG in short) considers galaxy formation and evolution through large-scale cos-mological hydrodynamical simulations (????????). Such

We provide a Jupyter notebook to facilitate this fit here: https://github.com/LiekeVanSon/SFRD_fit/ blob/main/src/scripts/Notebooks/Fit_model_to_sfrdzZ. ipynb

simulations provide the tools to study parts of the Universe that are not easily accessible by observations. In particular of interest for this work, they simulate the high redshift enrichment of galaxies and the tail of low metallicity star formation at low redshift.

The models implemented in the publicly available TNG simulations $(?)^3$ have lead to many successes. These models where calibrated at the resolution of the 236 TNG100 simulation, hence TNG100 is expected to provide the best overall agreement to global properties (like 238 the star formation rate density). This is why we adopt 239 the TNG100 simulation as our fiducial simulation. For a more extended discussion focused on the processes that 241 govern the creation, distribution and mixing of metals 242 in in the TNG simulations, we refer to ?. In short, star ²⁴³ formation in the TNG simulations is calibrated against the Kennicutt-Schmidt relation (??), using an effective 245 equation of state (?). The stellar metallicity yields are 246 an updated version of the original Illustris simulations 247 as described in ?. Star particles deposit metals into the 248 gas through type Ia and type II supernovae, as well as 249 through asymptotic giant branch stars. The TNG sim-250 ulations have been shown to match observational constraints on the mass-metallicity relation of galaxies up 252 to z=2 (?), as well as iron abundances (?), metallicity 253 gradients within galaxies at low redshift (?), and the reduction of star formation in the centers of star-forming 255 galaxies (?). Several studies have used the TNG simulations to make predictions for astronomical transient sources (e.g. ???). Out of the four S(Z,z) variations ex-258 plored, ? find that TNG provides one of the best agree-²⁵⁹ ments between observed and predicted cosmic rates for 260 electromagnetic and gravitational-wave transients, when 261 combined with their fiducial binary population synthesis

On the other hand, large uncertainties and crude approximations remain in all contemporary cosmological simulations, thus also in the TNG simulations. Generally, some of the chemical evolution of galaxies in cosmological simulations is unresolved, and thus depends strongly on the implemented 'sub-grid physics'. A known uncertainty is that dust is not included in the TNG simulations, which could mean that metallicity of the star-forming gas is overestimated. Feedback from active galactic nuclei is not well understood theoretically and is described in an approximate manner (??). Furthermore, all stellar winds mass loss from massive stars, binary interactions and their ionising effects are ignored (e.g. ???????). Moreover, the uniform ionising UV back-

277 ground is turned on abruptly at z=6. This crucially 278 impacts the amount of low metallicity star formation 279 at high redshift as it allows small galaxies to produce 280 more stars than what would be expected for a gradually 281 increasing UV background that reaches full strength at 282 z=6. All these uncertainties underline the need for a 283 flexible approximation of the $\mathcal{S}(Z,z)$, that can be easily updated when cosmological models and sub-grid physics 285 are updated.

3.2. Choices and binning of the data

We fit equation 1 to the metallicity-dependent star formation rate of the star-forming gas in the TNG100 simulation. For this we use a binned version of the TNG data $S(Z,z)_{\rm sim}$. We consider metallicities between $\log_{10} Z = -5$ to $\log_{10} Z = 0$ in 30 bins, where we use $\log_{22} Z_i$ to refer to the logarithmic centres of the bins. We gignore star formation in metallicities $\log_{10} Z \leq -5$ as formation rate in these simulations. We consider bins in redshifts between z=0 and z=10, with a step size of dz=0.05, where z_j refers to the centres of the bins.

3.3. Optimisation function

To find a solution we use a method based on the sum of the quadratic differences between the simulations and our fit function. Using a vanilla χ -squared approach does not serve our purposes very well as it does a poor job in fitting regions where the star formation is very low. Using a χ -squared approach on the logarithm of the function instead places far too much weight on trying to fit the star formation rate in regions where the rate is very low or not even significant. After experimenting, we find that the following approach gives us satisfactory results.

We first consider a given redshift z_j . For this redshift we compute the sum of the squared residuals between the cosmological simulation and our fit. This is effectively the square of the l^2 -norm:

$$\chi^2(z_j) \equiv \sum_{Z_i} \left(\mathcal{S}(Z_i, z_j)_{\text{sim}} - \mathcal{S}(Z_i, z_j)_{\text{fit}} \right)^2. \tag{13}$$

Here, the variable Z_i runs over all metallicity bins. We are particularly interested in properly fitting the low metallicity star formation at high redshifts. At high redshifts, the overall star-formation rate density is generally lower. To ensure that our fitting procedure gives sufficient weight to the behaviour at all redshifts, we introduce a penalisation factor to somewhat reduce the contribution of redshifts where the peak of cosmic star formation occurs, while increasing the weight at redshifts where the overall star-formation rate density is

³ https://www.tng-project.org/

325 lower. To achieve this we divide $\chi^2(z_j)$ by the star for-326 mation $\sum_{Z_i} \mathcal{S}(Z_i, z_j)$ per redshift bin before adding the 327 contribution of all redshifts. Our final expression for the 328 cost function reads

$$\chi = \sum_{z_j} \frac{\chi^2(z_j)}{\sum_{Z_i} \mathcal{S}(Z_i, z_j)}$$
 (14)

To minimize this cost function, we use scipy optimize minimize from SciPy v1.6.3 which implements the quasi-Newton method of Broyden, Fletcher, Goldfarb, and Shanno (BFGS, ?).

3.4. Resulting S(Z, z)

334

Our best fitting parameters are listed in Table 1. With these fit parameters, $\chi^2(z_j)$ is smaller than $2 \cdot 10^{-4}$ at any given redshift. To evaluate our fit, we show the residuals in Appendix A. We will refer to the $\mathcal{S}(Z,z)$ with the parameters listed in Table 1 as our fiducial model.

In Figure 1 we show our fiducial model at different redshifts and metallicities. We also show the overall starformation rate density SFRD(z) in Figure 2. In general,
our analytical model captures the metallicity-dependent
cosmic star formation history in the TNG100 simulations well (bottom panels of Figure 1). The skewedlog normal metallicity distribution is able to reproduce
the overall behaviour that is observed in TNG100 (bottom left panel, but cf. ?, for an in-depth discussion
of low metallicity star formation in the TNG50 simulation). Only minor features like the additional bump just
above $\log_{10}(Z) = -2$ at redshift 2 are missed. However,
for our purposes, it is more important to prioritise fitting the large scale trends, while we are not so interested
in smaller scale fluctuations.

Adopting a skewed-lognormal metallicity distribution allows for a tail of low metallicity star formation out to low redshifts. To emphasise the difference between a skewed-lognormal and a symmetric lognormal distribution, we show the phenomenological model from a functions, we show the phenomenological model from functions that is encompassed by our model described in Section 2, but we note that their model is distinctly different.

Although our model preforms well at reproducing the large scale trends seen in TNG, we acknowledge that

367 more complex features as suggested by some observa-368 tional studies could be missed. One example is that 369 the SFRD(z) shape we adopt from ? does not account 370 for starburst galaxies (see discussion in?). Moreover, 371 our model cannot capture inflection points in the mean metallicity, because we assume both μ_0 and μ_z are con-373 stants with redshift (equation 7). Contrarily, ? find an 374 upturn in the amount of low metallicity star formation 375 above z = 4 if the power law of the GSMF is allowed 376 to evolve with redshift. Hence, although our model is 377 more broadly applicable than previous models, in it's 378 current form, it does not capture the complete range of 379 observationally-allowed variations. Incorporating more 380 complex functional forms for our the mean metallicity 381 could possibly capture such behaviour, but this analysis 382 is beyond the scope of this paper.

383 4. APPLICATION: SYSTEMATIC VARIATIONS OF $\mathcal{S}(Z,z)$ AND THE EFFECT ON THE MASS DISTRIBUTION OF MERGING BBHS

We will now demonstrate the application of our analytical model by systematically varying the parameters in our fiducial S(Z,z) model, and investigate their effect on the local mass distribution of BBH mergers originating from isolated binaries.

We use the publicly available rapid binary population synthesis simulations presented in ?.⁵ These simulations were run using version v02.26.03 of the open source COMPAS suite (?)⁶. COMPAS is based on algorithms that model the evolution of massive binary stars following ?? using detailed evolutionary models by ?. In particular, we use the simulations behind Figure 1 from ?, and we refer the reader to their methods section for a detailed description of the adopted physics parameters and assumptions. Metallicities of each binary system were sampled from a smooth probability distribution to avoid artificial peaks in the BH mass distribution (e.g. ??). These simulations provide us with an estimate of the yield of BBH mergers per unit of star-forming mass and metallicity.

We combine the aforementioned yield with variations of the fiducial S(Z,z) model described in this work. By integrating over cosmic history, we obtain the local merger rates of BBH systems, which allow us to con-

⁴ The phenomenological model from ? is recovered by adopting $\mu_0=0.035,\ \mu_z=-0.23,\ \omega_0=0.39,\ \omega_z=0,\ \alpha=0,\ a=0.01,\ b=2.77,\ c=2.9$ and d=4.7.

 $^{^5}$ Available for download at https://sandbox.zenodo.org/record/ $1101303,\,\rm see$ also the Software and Data section in the acknowledgements

 $^{^6}$ https://github.com/TeamCOMPAS/COMPAS

⁷ We note that the rate in ? is slightly higher than the fiducial rate presented in Figure 3 in this work. This difference is caused by the use of rounded parameter values of S(Z,z) in ?.

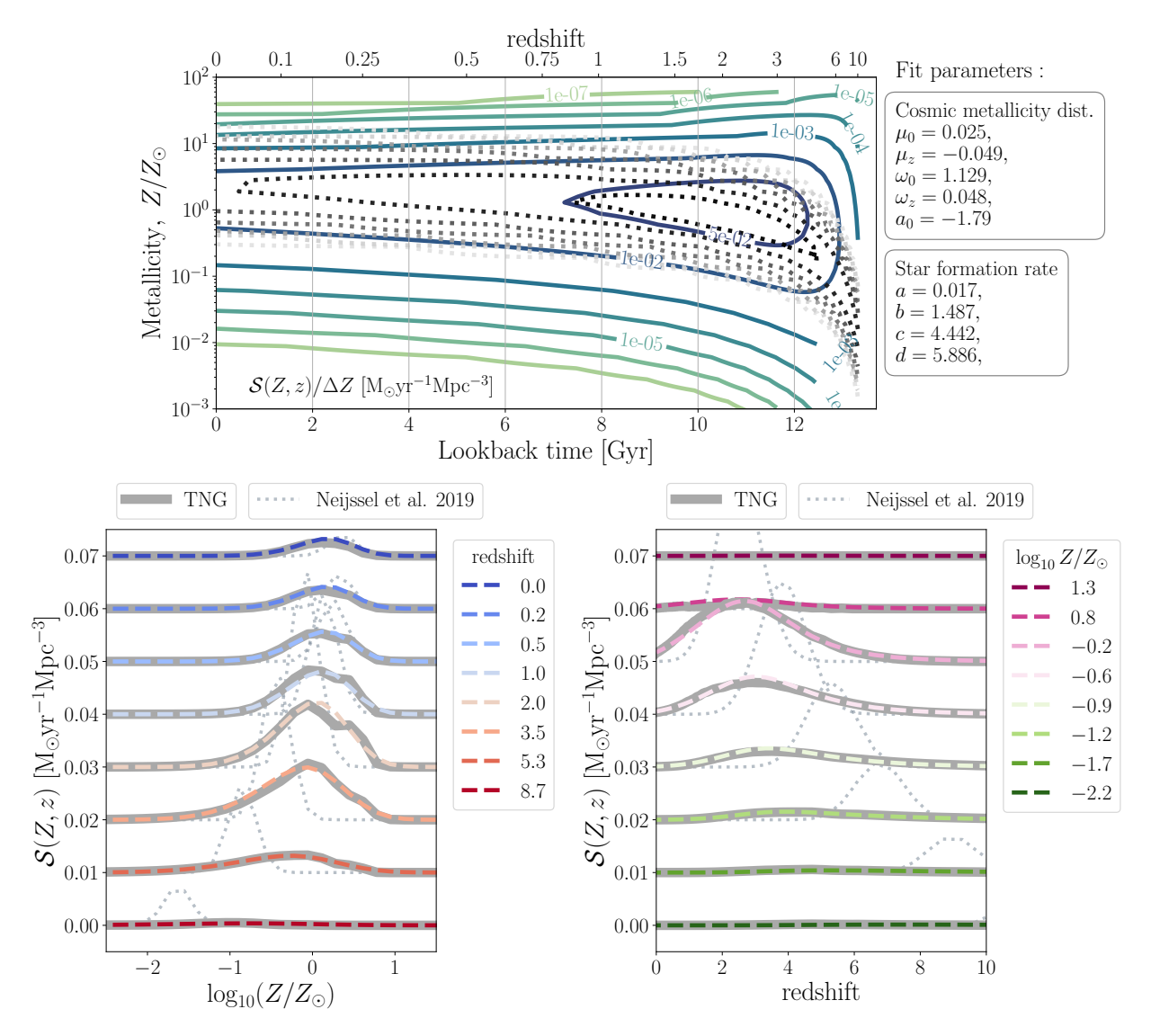


Figure 1. Our fiducial S(Z, z) model, adopting the best fitting parameters (listed on the top right) to fit the TNG100 simulations. The top panel shows the full two dimensional S(Z, z) linear in time. Contours range from $10^{-7} - 10^{-2} \text{M}_{\odot} \text{ yr}^{-1} \text{ Mpc}^{-3}$. The bottom left (right) panel shows slices of the distribution in redshift (metallicity). Each slice is displaced by $0.01 \text{M}_{\odot} \text{ yr}^{-1} \text{ Mpc}^{-3}$ (note the linear scale of S(Z, z) in the bottom panel). We show the TNG100 simulation data with thick gray lines. For comparison, we also show the phenomenological model from ? in all panels with grey dotted lines. The bottom panels show that our analytical model adequately captures the shape of the S(Z, z) from TNG100.

struct the distribution of source properties at every redshift. We use the cosmic integration scheme that is part
of the publicly available COMPAS suite, which includes
the S(Z,z) model described in this work. The details of this framework are described in ?, but also in ?,
where more similar settings to this work are used.

4.1. Determining reasonable variations of S(Z, z)

416

We consider variations in both the shape of the cosmic metallicity density distribution dP/dZ(Z,z), and the shape of the overall star-formation rate density, SFRD(z). To determine the range that is reasonably allowed by observations, we compare our variations to the $\mathcal{S}(Z,z)$ models described in ?. An overview of the explored variations is shown in Table 2. Below we explain how we arrive at these values.

For the cosmic metallicity density distribution, we vary every parameter that determines the shape of dP/dZ(Z,z) independently (three left-most columns of Table 1, and top of Table 2), while keeping all other parameters fixed at their fiducial value. For each variation, we inspect the fraction of stellar mass that is formed at low-metallicity ($Z < 0.1Z_{\odot}$) versus the fraction of stellar mass that is formed at high-

dP/dZ	description	best fit	SFRD(z)	best fit
			$\rm M_{\odot}yr^{-1}Mpc^{-3}$	
μ_0	mean metallicity at $z = 0$	0.025 ± 0.036	a	0.02 ± 0.072
μ_z	z-dependence of the mean	-0.049 ± 0.006	b	1.48 ± 0.002
α	shape (skewness)	-1.778 ± 0.002	c	4.44 ± 0.001

 1.122 ± 0.001

 0.049 ± 0.009

d

Table 1. Best fitting parameters for our S(Z, z) fit to TNG100 data.

Table 2. Variations on S(Z,z). For every variation, we either swap the value of an individual $\mathrm{dP}/\mathrm{dZ}(Z,z)$ parameter, or exchange the set of four $\mathrm{SFRD}(z)$ parameters, and replace them by the the min/max values listed here. All other parameters are kept fixed at their fiducial value.

 ω_0

 ω_{γ}

scale at z = 0

z-dependence of the scale

	min	fiducial	max
dP/dZ(Z,z)			
μ_0	0.007	0.025	0.035
μ_z	0.0	-0.049	-0.5
α	-6.0	-1.778	0.0
ω_0	0.7	1.125	2.0
ω_z	0.0	0.048	0.1
SFRD(z)			
$(a,b \dots$	(0.01, 2.60)	(0.02, 1.48)	(0.03, 2.6)
\dots $c,d)$	3.20, 6.20)	4.44, 5.90)	3.3, 5.9)

metallicity ($Z>Z_{\odot}$), for all star formation that occurred below a certain threshold redshift. We compare this to the models from ? in Figure 6 in Appendix B. We have chosen our variations such that they span a reasonable range of cosmic metallicity density distributions as allowed by observation-based and cosmological simulations-based models. We use the models 214-f14SB-BiC_FMR270_FOH_z_dM.dat, and 2302-f14SB-Boco_FMR270_FOH_z_dM.dat from ?⁸ as a representation of a very low and high metallicity star formation realisation respectively. These models are the low and high metallicity extreme under their fiducial SFR-metallicity correlation, and so we will refer to them as Chr21_lowZ and Chr21_highZ respectively 448 from hereon. The difference between these mod-449 els lies in the assumptions in the underlying em-450 pirical galaxy relations. In general, low-mass 451 galaxies contribute to low-metallicity star forma-452 tion and shift the peak of S(Z,z) to lower metal-453 licities. Chr21_lowZ is characterised by a star for-454 mation-galaxy mass relation that is flat at high 455 galaxy masses (reducing the star formation rate 456 for the highest-mass galaxies), a galaxy stellar 457 mass function that evolves with redshift (pre-458 dicting an increasing number density of low-mass 459 galaxies), and a local galaxy mass-metallicity re-460 lation as in?. This model further approximates 461 the contribution of starburst galaxies following? 462 and ?. Assuming that starburst galaxies follow 463 the empirical fundamental metallicity relation 464 (leading to anti-correlation between the SFR and 465 metallicity), their inclusion tends to shift the 466 peak of S(Z,z) to lower metallicities and broad-467 ens the low-metallicity part of the distribution. 468 On the other hand, Chr21_highZ assumes the star 469 formation-galaxy mass relation does not flatten 470 towards higher galaxy masses, a galaxy stellar 471 mass function where the slope for the low-mass 472 end is constant over redshift, and a local galaxy 473 mass-metallicity relation following?. Lastly, this 474 model adopts the starburst prescription from ?, which produces results that are similar to models 476 without starburst galaxies.

 5.90 ± 0.002

For every variation of our model, we inspect both the full $\mathcal{S}(Z,z)$ and slices at redshifts z=0,0.5,3.0 and 6 by eye. At each slice we compare our model variation to Chr21_lowZ and Chr21_highZ, and ensure that none of our variations significantly exceeds these extremes in $\mathcal{S}(Z,z)$. This also serves as a sanity check for the overall star-formation rate density.

We also consider two variations of the overall starformation rate density, SFRD(z), where we keep the metallicity distribution dP/dZ(Z,z) fixed, but vary all

⁸ These models including a detailed description of their contents are publicly available at https://ftp.science.ru.nl/astro/mchruslinska/Chruslinska_et_al_2021/

four SFRD(z) parameters at once (right two columns of Table 1, and bottom of Table 2). We use Figure 11 from ? to determine approximate upper and lower bounds to the overall star-formation rate density. We choose ? as an approximation of the lower limit. For the upper limit, we use the upper edge of models that adopt starbursts following ? and ? (SB: B18/C17), combined with a non-evolving low-mass end of the galaxy stellar mass function (shown as a thick brown line in Fig. 11 of ?, and described in their table B1). To approximate these models, we fit equation the power law description of this model as presented in appendix B1 of ?. We show all SFRD(z) variations in Figure 2.

502 4.2. The effect of the $\mathcal{S}(Z,z)$ on the primary masses of merging BBH

To isolate the effect of the S(Z,z) from the effects of different formation channels, we split the data from ? between the stable mass transfer channel (e.g., ??????), and the 'classical' common-envelope channel (or CE channel, e.g., ????). These channels are distinguished based on whether the binary system has experienced a common envelope phase (CE channel) or only stable mass transfer (stable channel in short from now on).

In Figures 3 and 4, we show the resulting primary mass distribution of merging BBHs from the stable channel and CE channel respectively. The primary (secondary) component refers to the more (less) massive component of merging BBHs. Each panel varies one aspect of the $\mathcal{S}(Z,z)$. In the first five panels of Figures 3 and 4, we vary one of the parameters that determine the shape of the probability density distribution of metallicities, while keeping all other values fixed at their fiducial values. In the last panel of Figures 3 and 4, we vary the shape of the overall star-formation rate densities, SFRD(z), to one of the variations shown in Figure 2, while keeping the probability density distribution of metallicities fixed.

The first thing we note is that the location of the features in the primary mass distribution are robust against variations in $\mathcal{S}(Z,z)$. For the stable channel, two features are visible in all variations: a peak at $M_{\rm BH,1} \approx 9 \rm M_{\odot}$ and a bump at $M_{\rm BH,1} \approx 22 \rm M_{\odot}$. Two more features are visible in at the high mass end for almost all $\mathcal{S}(Z,z)$; a knee at $M_{\rm BH,1} \approx 35 \rm M_{\odot}$ and another bump at $M_{\rm BH,1} \approx 45 \rm M_{\odot}$. Although the locations of these features are constant, the features themselves can disappear for variations that suppress the rate of high mass BHs (e.g., dashed lines in the top panels of Fig.

 $_{538}$ 3). Similarly, the CE channel displays a kink in the dis- $_{539}$ tribution at about $9{\rm M}_{\odot}$, and a peak at approximately $_{540}$ $M_{\rm BH,1} \approx 17{\rm M}_{\odot}$ for all variations. The latter peak is $_{541}$ the global peak of the mass distribution in almost all $_{542}$ variations.

The finding that the locations of features in the mass distribution do not change for different S(Z,z) is consis-545 tent with earlier work. Recent work by ? showed that, when comparing two very different models of $\mathcal{S}(Z,z)$ 547 (their Figure 5), the location of the peaks remains the 548 same, even though the normalisation between the two 549 BBH merger rates is completely different. Furthermore, 550 ? show the probability distribution of chirp masses for 551 BBHs in their Fig. 4. Although features can disappear when the S(Z,z) prohibits the formation of certain (typ-553 ically higher) mass BHs, the *location* of features remains 554 the same. This implies that the locations of features in 555 the mass distribution of BBHs are determined by the 556 formation channel and its underlying stellar and binary 557 physics. The locations of features could therefore serve 558 as sign posts of the underlying physics.

Second, we see that the low mass end of the pri-560 561 mary mass distribution is relatively robust against vari-₅₆₂ ations in S(Z,z). To quantify this, we annotate the ⁵⁶³ ratio between the maximum and minimum rate at three reference masses; $M_{\rm BH,1}=10,25,~{\rm and}~40{\rm M}_{\odot}.$ $M_{\rm BH,1} = 10 {\rm M}_{\odot}$, we find that the rate changes by at 566 most a factor of about 3.7 for the stable channel, and at most about a factor of 3.8 for the CE channel. On the 568 other hand, the change in rate at $M_{\rm BH,1}=40{
m M}_{\odot}$ can 569 be as high as a factor of about 200 and 150 for the stable 570 and CE channels, respectively. The lowest mass BHs are ₅₇₁ least affected by the S(Z,z) because they can be formed ₅₇₂ from all metallicities above $Z \gtrsim 10^{-3}$ (see e.g., Figures 573 7 and 13 from ?). The rate of star formation at metal-₅₇₄ licities above $\gtrsim 10^{-3}$ is observationally relatively well 575 constrained for redshifts below 0.5 (which comprises the 576 past 5 Gyr of star formation). This is reflected in the 577 top panel of Figure 6: all models show that 10% or less 578 of the stellar mass was formed at a metallicity below $_{579}$ $Z/10 \approx 0.0014$, or in other words, about 90% or more of 580 the stellar mass was formed at a metallicity above $\mathbb{Z}/10$. 581 Hence the lowest mass BHs derive from the least uncertain parts of the S(Z,z). The low-mass end of the mass 583 distribution of merging double compact objects will also 584 provide a particularly powerful cosmological constraint 585 in the era of third generation gravitational wave tele-586 scopes (?). Our finding that the low mass end is more robust against variations in S(Z, z) supports this claim. Parameter variations that affect shape of S(Z,z) at

589 low redshift primarily change the normalisation of the

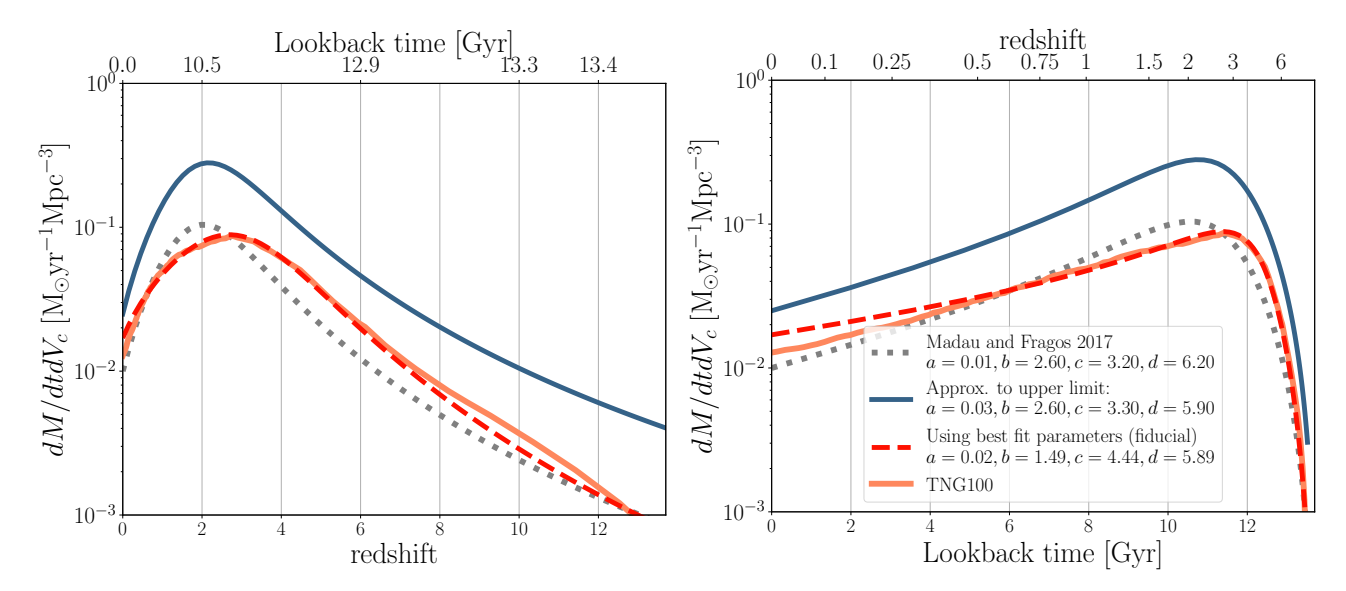


Figure 2. Comparison of several overall star-formation rate densities, SFRD(z), with redshift (left panel) and with lookback time (right panel). The solid orange and dashed red lines respectively show the star formation data from TNG100 and our corresponding fit adopting eq. 12 (fiducial model). The dotted gray and solid blue lines are variations of eq. 12 used to approximate the lower and upper edge of possible star-formation histories. The dotted gray line shows the model from ?, while the solid blue line mimics the behaviour of the powerlaw-fit to the SB: B18/C17 variations with a non-evolving low-mass end of the galaxy stellar mass function from ?.

590 mass distribution. This is the case for variations of the width of the cosmic metallicity density distribution at z = 0 (ω_0), the mean metallicity of the cosmic metallic-593 ity density distribution at z=0 (μ_0), and the skewness 594 of the cosmic metallicity density distribution (α , left 595 columns of Figures 3 and 4). To emphasise this point, 596 we annotate the total BBH merger rate at redshift 0.2, $\mathcal{R}_{0.2}$, in the legends of Figures 3 and 4 (0.2 is the redshift where the observations are best constrained?). Varia-599 tions that increase the amount of star formation at low metallicity (i.e. for a low mean metallicity $\mu_0 = 0.007$ and a wide metallicity distribution $\omega_0=2.0$) increase 602 the predicted BBH merger rate. This is consistent with 603 other work that finds merging BBHs form more effi-604 ciently at low metallicities (e.g. ?????). A more skewed 605 cosmic metallicity density distribution pushes the peak 606 of the distribution to higher metallicities and thus forms more stars at high metallicity when compared to a symmetric distribution. Hence, the local rate of BBH merg-609 ers is lower for the skewed distribution ($\alpha = -6$) with for respect to the symmetric variation ($\alpha = 0.0$).

Changing the overall star-formation rate density (SFRD(z), bottom right panels of Figures 3 and 4) also affects the normalisation of the mass distribution, but has a smaller effect than the width and the mean of the cosmic metallicity density distribution at z=0 (ω_0 and μ_0). This underlines the importance of the amount of low-metallicity star formation (e.g., ?), and is furthermore in line with findings from ?. As discussed in Sec-

tion 4.1, we use ? and the solid blue line in Figure 2 as an approximate lower and upper bound to the SFRD(z) respectively. The overall cosmic star formation rate density from ? is very similar to our fiducial model (Figure 2), and the differences between the resulting mass distributions are correspondingly small. Our approximation of the upper limit to the allowed SFRD(z) leads to an overall increase of the BBH merger rate by a factor of about 3.

Parameters that change the evolution of the metallic-629 ity distribution dP/dZ(Z,z) with redshift, such as the 630 redshift dependence of the with and mean; ω_z and μ_z 631 (top right and centre right panels of Figures 3 and 4) 632 primarily affect the high mass end of the stable channel. 633 We understand this as an effect of the different delay 634 time distributions for both formation channels. Since both, ω_z and μ_z influence the amount of low metallicity 636 stellar mass formed at high redshifts they will mostly af-637 fect systems with longer delay times. The stable channel 638 has been shown to produce more high mass BHs with 639 longer delay times when compared to the CE channel 640 (??). Hence we find these variations affect the slope of 641 the high mass end of the BBH mass distribution for the 542 stable channel, while they have a relatively small impact 643 on the CE channel.

5. DISCUSSION & SUMMARY

We present a flexible analytic expression for the metallicity-dependent cosmic star formation history, $\mathcal{S}(Z,z)$ (equations 1, 11 and 12). An analytical expres-

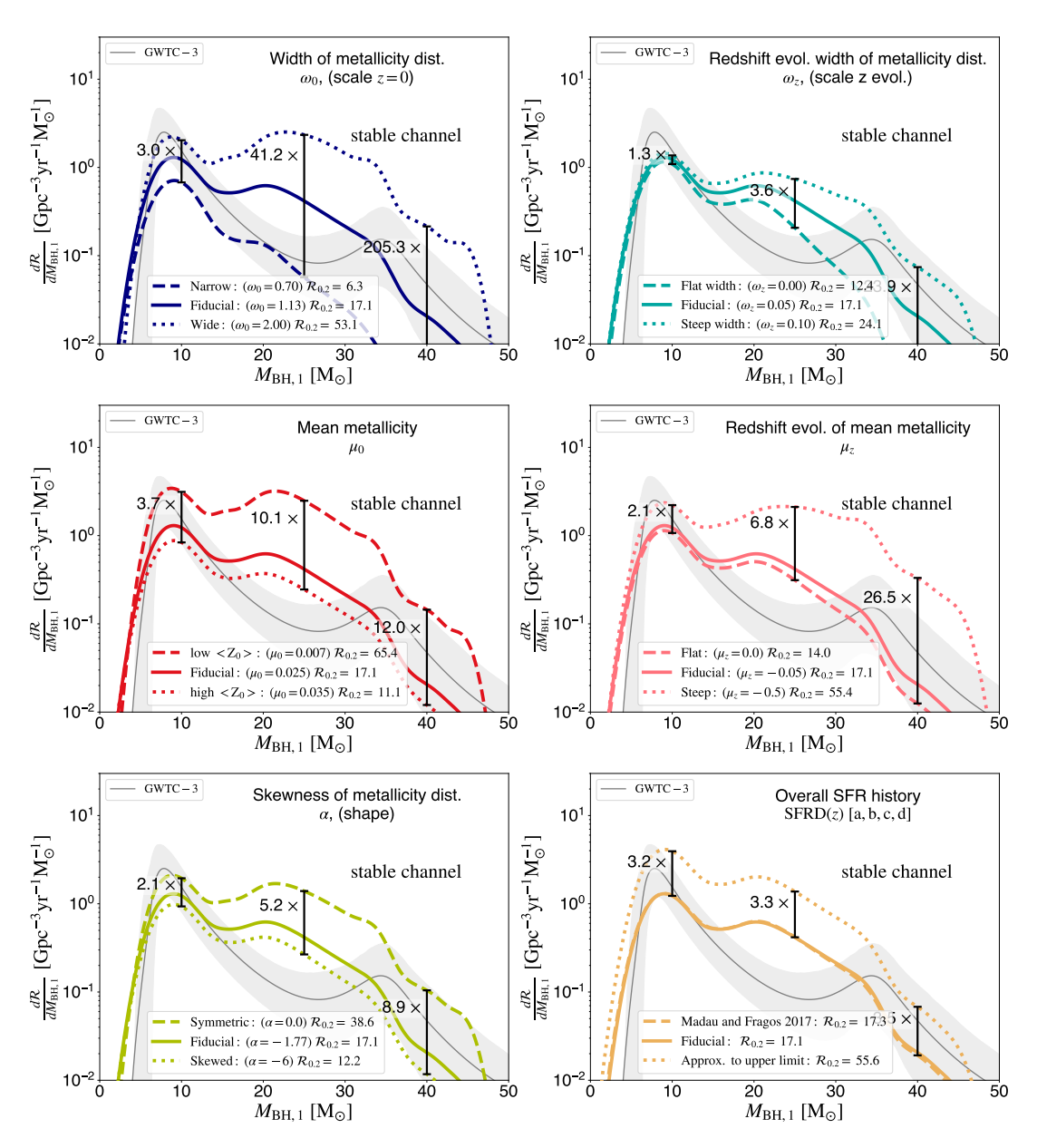


Figure 3. The primary mass distribution of merging BBH systems from the stable mass transfer channel for several variations in S(Z, z). The first five panels show variations of the cosmic metallicity density distribution dP/dZ(Z, z), eq. 11, (parameters listed in the first three columns of Table 1), where we vary one parameter at a time while keeping the rest fixed at their fiducial value. The bottom right panel shows variations in the magnitude of the star formation rate with redshift; i.e. SFRD(z). For the latter we vary the four fiducial parameters of SFRD(z) simultaneously (last two columns of Table 1). All panels are shown at a reference redshift of z = 0.2, with the corresponding predicted BBH merger rate indicated in the legend. For reference, we show the power-law + peak model from ? in grey. We annotate the relative change in the rate at three reference masses: $10M_{\odot}$, $25M_{\odot}$ and $40M_{\odot}$.

 $_{648}$ sion allows for controlled experiments of the effect of $_{649}$ $\mathcal{S}(Z,z)$ on dependent values, such as the rate and mass $_{650}$ distribution of merging BBHs. The model presented in $_{651}$ this work adopts a skewed-lognormal for the distribution $_{652}$ of metallicities at every redshift $(\mathrm{dP/dZ}(Z,z))$.

The model can capture the general behaviour of cosmological simulations, such as TNG100—Our analytical expression

for $\mathcal{S}(Z,z)$ is composed of a cosmic metallicity density distribution that is determined by a mean, scale and standard skewness and their redshift dependence, as well as parameters governing the overall star-formation rate density. We fit our analytical expression for $\mathcal{S}(Z,z)$ to the star-forming gas in the TNG100 simulation, and provide the best fit parameters in Table 1. We show that our model captures the shape and general behaviour of the

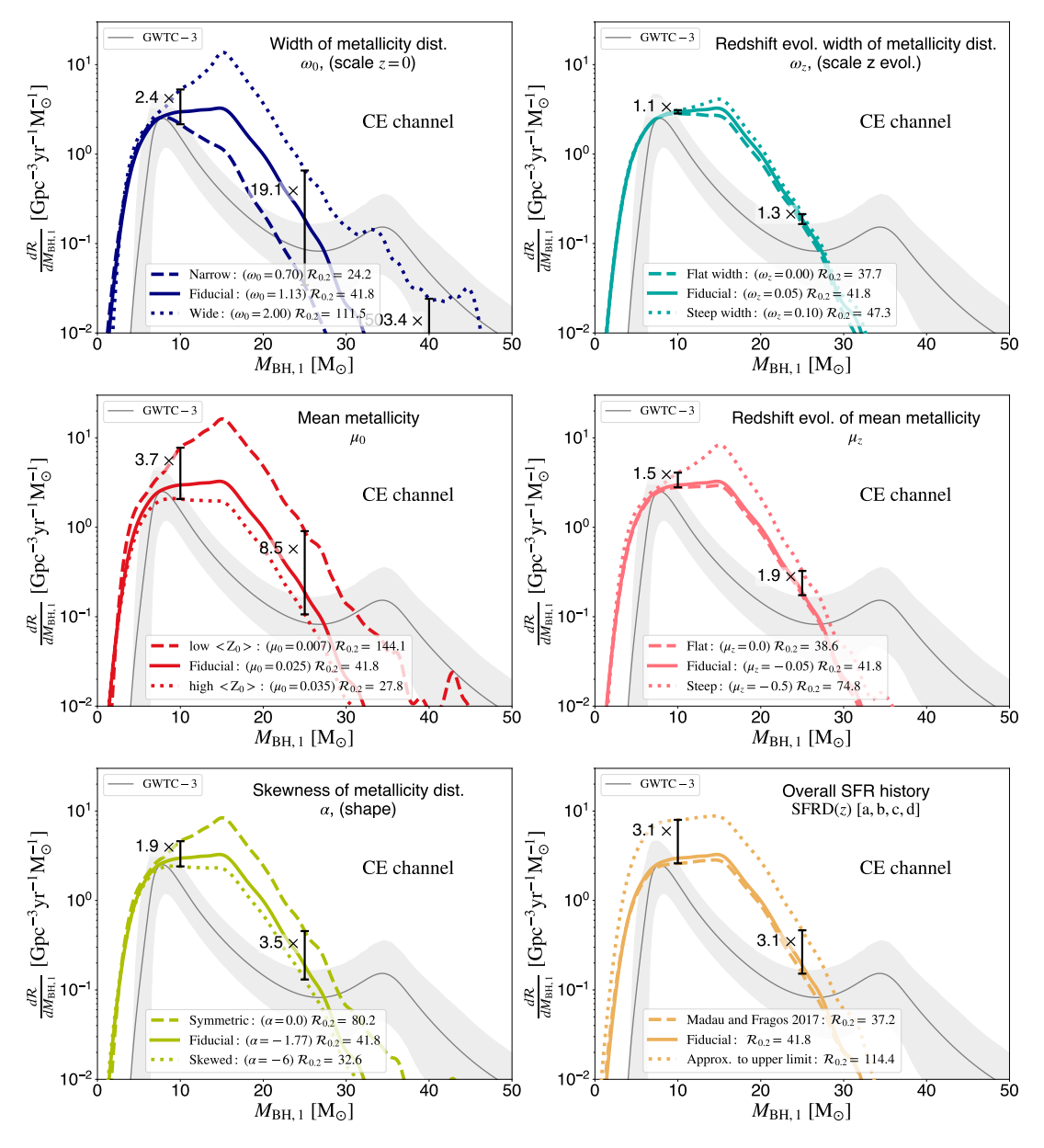


Figure 4. Same as Figure 3, but for the Common Envelope channel. These figures show that the low mass end of the primary mass distribution is least affected by the adopted S(Z, z). Moreover, the *location* of features in the mass distribution are robust against all explored variations.

680

681

682

683

684

685

cosmological simulations well (Figure 1). Although our model is more broadly applicable than previous models, we acknowledge that it does not capture the *complete* range of observationally-allowed variations in it's curfor rent form. Incorporating more complex functions for the redshift evolution of the metallicity could solve this is issue, but this is left for future research.

The model allows for a controlled experiment on the effect of S(Z,z) on the local distribution of merging BBH—As an erg example, we use our model to calculate the local rate and mass distribution of the more massive components from merging BBHs $(M_{\rm BH,1})$ in Figures 3 and 4. We

 $_{676}$ systematically vary all five parameters that shape the $_{676}$ cosmic metallicity density distribution, and explore two $_{677}$ additional variations of the overall star-formation rate $_{678}$ density SFRD(z). Our main findings are as follows:

- The locations of features in the distribution of primary BH masses are robust against variations in S(Z, z). The location of features in the mass distribution of BHs could thus be used as sign posts of their formation channel.
- For all variations, the low mass end of the mass distribution is least influenced by changes in the

687

689

690

691

693

694

695

696

697

698

700

701

702

703

704

705

706

707

708

744

745

S(Z,z). This is because the lowest mass BHs can be formed from all metallicities above $Z\gtrsim 10^{-3}$, for which the star formation rate is relatively well constrained in the recent Universe. This suggests that the lower end of the BH mass distribution (component masses of $\leq 15 {\rm M}_{\odot}$) is potentially very powerful for constraining the physics of the formation channels, irrespective of the cosmic star formation rate uncertainties.

- The metallicity distribution of star formation at low redshift primarily impacts the normalisation of the BBH merger rate. Changing the overall star-formation rate density, SFRD(z) also affects the rate, but to a lesser degree. This shows that low-metallicity star formation at low redshifts dominates the overall normalisation of the BBH merger rate.
- Parameters that influence the redshift evolution of the mean and the width of the metallicity distribution affect the slope of the high mass end of the primary BH mass distribution for the stable channel. This reflects the longer delay times of the stable channel with respect to the CE channel.

The flexibility of the model presented in this work can capture the large uncertainties that remain in the shape and normalisation of the metallicity-dependent cosmic star formation history. Our hope is that this expression will provide a useful starting point for making predictions and comparisons with observations.

The authors acknowledge partial financial support from the National Science Foundation under Grant No. (NSF grant number 2009131 and PHY-1748958).", the Netherlands Organisation for Scientific Research (NWO) as part of the Vidi research program BinWaves with project number 639.042.728 and the European Union's Horizon 2020 research and innovation program gram from the European Research Council (ERC, Grant agreement No. 715063). This research was supported in part by the National Science Foundation under Grant No. NSF PHY-1748958.

SOFTWARE AND DATA

All code associated to reproduce the data and plots in this paper is publicly available at https://github. com/LiekeVanSon/SFRD_fit. The data used in this work is available on Zenodo under an open-source Creative Commons Attribution license at 10.5072/zen-do odo.1101303. All observationally constrained models of the $\mathcal{S}(Z,z)$ from ? can be found online at: https://ftp.science.ru.nl/astro/mchruslinska/ Chruslinska_et_al_2021/.

This research has made use of GW data provided by the Gravitational Wave Open Science Center (https://www.gw-openscience.org/), a service of LIGO Laboratory, the LIGO Scientific Collaboration and the Virgo Collaboration. Further software used in this work: Python (?), Astropy (??) Matplotlib (?), NumPy (?), SciPy (?), ipython/jupyter (??), Seaborn (?) and hdf5 (?).

APPENDIX

A. EVALUATING OUR FIT; THE SQUARED RESIDUALS

In Figure 5 we show the \log of the squared residuals. The residuals are the content of the sum region 13, which is used in the cost function, equation 14, to optimise our fit. We see that the maximum residuals appear just below the peak of star formation. We note that we chose to

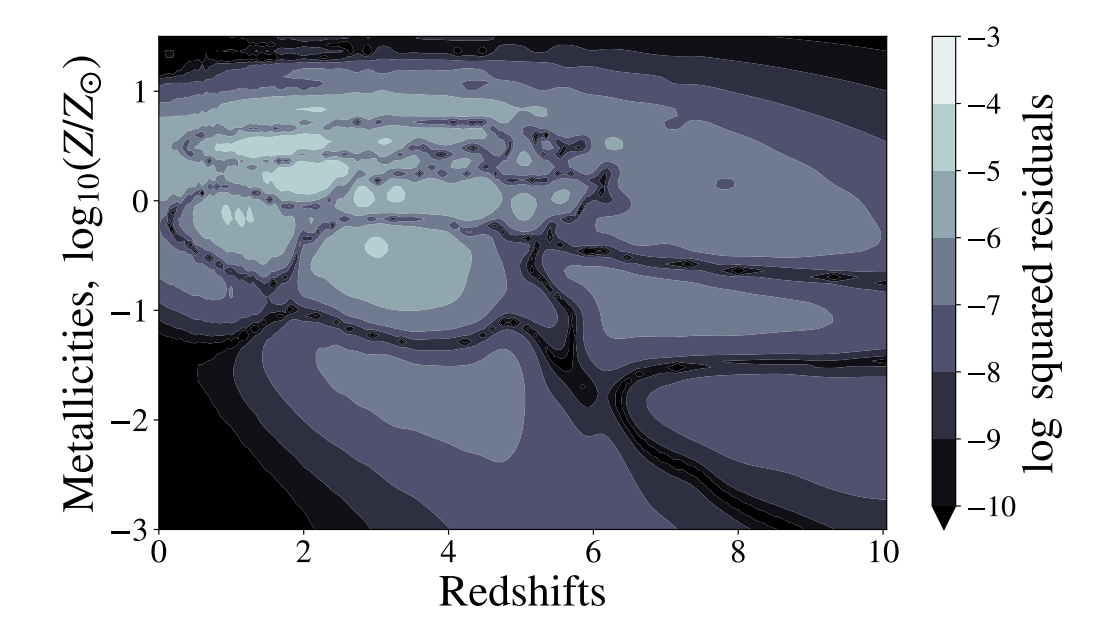


Figure 5. log of the squared residuals, which appear in equation 14 to optimise our fit.

minimise the squared residuals (which is similar to minimising the mean squared error) in favour of e.g. minimising the relative error, to prevent overfitting regions of very low star-formation rate.

B. DETERMINING REASONABLE VARIATIONS OF THE $\mathcal{S}(Z,z)$

751

To determine reasonable variations of our fiducial model for S(Z, z), we compute the fraction of low and high metallicity stellar mass formed for redshifts below z < 0.5, z < 3.0 and z < 10. We show the results in Figure 6, which results in an adaptation of Fig. 2 in ?, which in turn builds on Fig. 9 from ?.

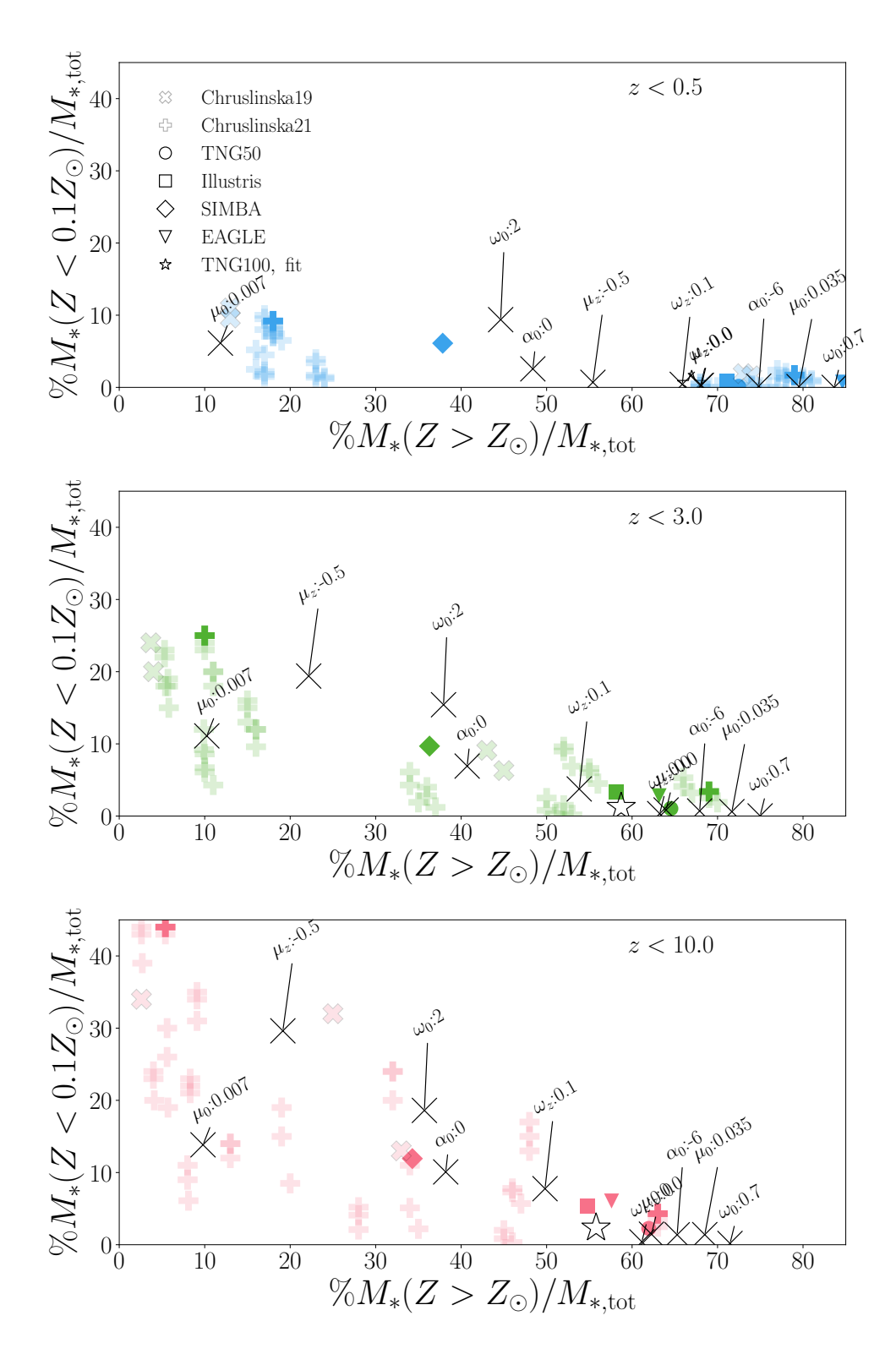


Figure 6. Percentage of stellar mass formed at low metallicity $(Z < 0.1Z_{\odot})$, versus high metallicity $(Z > Z_{\odot})$ for all star formation below a certain threshold redshift: z < 0.5 (top), z < 3.0 (middle) and z < 10 (bottom). Data from observation-based variations are shown with semi-transparent thick crosses, (?) and semi-transparent thick plus signs (?), the low- and high-metallicity extremes are indicated with opaque symbols. For data from cosmological simulations, we follow ? and show Illustris (?, squares), Simba (?, diamonds), EAGLE (?, triangles), TNG50 and TNG100 (?, filled and open circles respectively). Black thin crosses display variations of the cosmic metallicity density distribution that is part of our fiducial S(Z, z). The parameter that is varied with respect to the fiducial and its new value are annotated. This shows that our S(Z, z) variations span the range of reasonable cosmic metallicity density distributions as determined by observation-based and cosmological simulations-based models.